Structure, Magnetism, and Transport Properties of $Pr_{1-x}Sr_xMnO_3$ ($x = 0.45-0.75$) up to 1200 K

K. Knížek,* J. Hejtmánek, and Z. Jirák

Institute of Physics of ASCR, Cukrovarnická 10, 16253 Prague 6, Czech Republic

C. Martin, M. Hervieu, and B. Raveau

Laboratoire CRISMAT, UMR 6508, ISMRA, Bd du Maréchal Juin, 14050 Caen, France

G. André and F. Bourée

Laboratoire Léon Brillouin, CEA/Saclay, 91191 Gif-sur-Yvette, France

Received October 13, 2003. Revised Manuscript Received January 19, 2004

The perovskite manganites $Pr_{1-x}Sr_xMnO_3$ in the region $0.45 \le x \le 0.75$ exhibit two crystallographic modifications at room temperature—orthorhombic *Ibmm* and tetragonal *I*4/*mcm*—with boundary situated at $x \sim 0.48$. The high-temperature X-ray diffraction data show that for $x \ge 0.6$ the tetragonal phase of *I*4/*mcm* symmetry transforms on heating directly to the cubic *Pm*3*m* symmetry. On the other hand, for $x < 0.6$ the *I*4/*mcm* phase transforms successively to orthorhombic *Ibmm* through a two-phase region, then to rhombohedral $R\bar{3}c$, and finally to cubic *Pm*3*m*. The transient rhombohedral $R\bar{3}c$ phase is present also for orthorhombic compounds $Pr_{1-x}Sr_xMnO_3$ with $x < 0.48$. High-temperature structural transitions are not associated with any observable anomalies in electrical transport and paramagnetic properties while the occurrence of three magnetically ordered phases (FM, A-type and C-type AFM) at low temperature influence resistivity and thermopower essentially.

Introduction

The perovskite manganites with nonintegral mean valence (Mn^{3+}/Mn^{4+}) are materials of a great diversity of the structural, magnetic, and electric properties (see, for example, ref 1). Recent prospects are mainly associated with an occurrence in some manganites of a ferromagnetic and metallic state, in which charge carriers appear to be fully spin-polarized. This is ideal for spin-injection and spin-tunneling devices. Alternatively, the conducting spin-aligned phase can be induced by an external field, leading to a colossal magnetoresistance. Unfortunately, the technological potential of magnetotransport effects is still limited by the ferromagnetic Curie temperatures that only exceptionally exceed room temperature. Another domain of eventual applications relies on the chemical stability and concerns the thermoelectric properties at elevated temperatures, that is, in the paramagnetic state. Indeed, some perovskite and perovskite-related manganites are considered as promising n-type high-temperature thermoelectric materials for use in thermoelectric batteries, especially in combination with p-type cobaltites.[2] The essential characteristics required for such application are the high thermoelectric power and good electric conductivity while the thermal conduction should be depressed. This can be achieved by a tuning of chemical composition and control of sample granularity or texture. Furthermore, a great commercial importance represents the high-temperature applications of manganites as cathode materials in solid oxide fuel cells.[3] Their main advantages are thermodynamical stability, appreciable electronic conductivity, catalytic properties for the reduction of oxygen, resistance against chemical reactivity with solid oxide electrolytes, and simultaneously, a good matching of their thermal expansion coefficients. To obtain a satisfactory performance of both the cathode and electrolyte, high operating temperatures, ~1000 °C, and hydrogen as fuel are generally used. The economical costs demand, however, a lowering of temperatures by use of alternative fuels such as methanol (450−500 °C).[4] To conclude, there is an urgent need for engineering of new materials based on transition metal oxides, for which the knowledge of structural and physical properties of the prototype compounds in a broad temperature range is of prime importance.

Our contribution is focused on a detailed structural and magnetic description of manganites, $Pr_{1-x}Sr_xMnO_3$ ($x \sim 0.45-0.75$) which are characterized by perovskite structure of the orthorhombic *Ibmm* or tetragonal *I*4/*mcm* symmetry. The particular interest in this system is associated with the fact that the samples studied are situated just at the boundary between the narrow and

* Corresponding author. Fax: +420 233 343 184. E-mail: knizek@fzu.cz.

(1) Mathur, N.; Littlewood, P. *Phys. Today* **2003**, *56*, 25.
(2) Matsubara, I.; Funahashi, R.; Takeuchi, T.; Sodeoka, S.; Shimizu, T.; Ueno, K. *Appl. Phys. Lett.* **2001**, *78*, 3627.
(3) Skinner, S. J. *Int. J. Inorg. Mater.* **2001**, *3*, 113.
(4) Kostogloudis, G. Ch.; Vasilakos, N.; Ftikos, Ch. *J. Eur. Ceram. Soc.* **1997**, *17*, 1513.

10.1021/cm034997r CCC: $27.50
Published on Web 02/18/2004

wide electron band systems, the extremes being the antiferromagnetic charge-ordered insulators with the orthorhombic *Pbnm* symmetry (e.g., $Ln_{1-x}Ca_xMnO_3$) and the ferromagnetic metallic conductors with the rhombohedral $R\bar{3}c$ symmetry (e.g., $La_{1-x}Sr_xMnO_3$ for $x \leq 0.5$ or $La_{1-x}Na_xMnO_3$ for $x \leq 0.2$). The delicate balance between metallicity and localization is a reason for a rich magnetic phase diagram of $Pr_{1-x}Sr_xMnO_3$ at low temperatures.[5−8] In addition, a complicated sequence of crystallographic transitions is revealed at high temperatures. The present study provides data on the phase transitions, lattice parameters, and paramagnetic susceptibility up to 1200 K. This includes also the determination of ordered magnetic moments for three low-temperature phases with distinct character of carriers—the FM phase for $x \leq 0.48$ with a metallic (three-dimensional) conductivity, the A-type (layered) AFM phase which in its pure form for $x \sim 0.55-0.57$ becomes metallic (two-dimensional) in the layers,[9] and finally, the C-type (chain) AFM phase for $x > 0.6$ with polaronic conductivity preferentially along the chains (quasi-one-dimensional).[6] For selected compounds, the results are complemented with the resistivity and thermopower data.

Experimental Section

Samples $Pr_{1-x}Sr_xMnO_3$ ($x = 0.45-0.75$) were prepared by thoroughly mixing Pr_6O_{11}, $SrCO_3$, and MnO_2 in stoichiometric proportions. The mixtures were first heated at 1000 °C three times with intermediate grindings to achieve decarbonation. Powder was pressed in the form of pellets under 1 ton/cm^2 and sintered at 1500 °C for 12 h in air. The samples were then cooled at 5 °C min^{-1} down to 800 °C and finally quenched to room temperature.

Neutron experiments were carried out at the LLB (Saclay, France) on the G41 diffractometer using a wavelength of $\lambda = 2.4266$ Å to determine the temperature evolution of nuclear and magnetic structures. Samples were first cooled to helium temperature and patterns were recorded over an angular range $17° \leq 2\theta \leq 97°$ by warming from 2 K to room temperature. Additional measurements at 10 and 300 K were carried out on the high-resolution 3T2 diffractometer ($\lambda = 1.2251$ Å, $6° \leq 2\theta \leq 125°$). The high-temperature structural characterization in the range 300−1200 K was realized using the X-ray powder diffractometer Bruker D8 (Cu Kα) equipped with MRI TC wide-range temperature chamber. The measurements were performed under ambient atmosphere. Two scans were measured for each temperature and the measured intensities compared to check whether the sample has not changed during the measurement of one temperature. Both the X-ray and neutron diffraction patterns were analysed with the Rietveld method using the FULLPROF program (version Mar98-LLB JRC). The cationic compositions were determined by EDS (energy dispersive spectroscopy) analysis, using analyzers mounted on the transmission electron microscopes. The cationic distributions were found to be very homogeneous and the actual compositions were found to be identical to the nominal ones.

Measurements of the electrical resistivity and thermoelectric power were carried out between 20 and 900 K using two experimental setups. The low-temperature measurements were performed up to 310 K using a close-cycle refrigerator with experimental setup described previously.[10] For the high-temperature measurements the sample was placed on the ceramic sample holder centered in the small tubular furnace with precisely controlled temperature. The standard K-type thermocouples (chromel−alumel) were used for the monitoring of the temperature gradient around 5 K imposed across the sample by means of an additional small furnace. In both cases the four-point steady-state method for the electrical resistivity was applied. The magnetic susceptibility was measured on a SQUID magnetometer in the range up to 400 K using a dc field of 100 Oe while the high-temperature data up to 900 K were obtained using a Faraday balance in a field of 3000 Oe.

Results

Crystal Structure. The perovskites $Pr_{1-x}Sr_xMnO_3$ for $x = 0.48-0.75$ crystallize in tetragonal *I*4/*mcm* symmetry characterized by a rotation of the interconnected MnO_6 octahedra around the *c*-axis. For $x < 0.48$ the symmetry is orthorhombic *Ibmm* (*Imma* in the standard setting) characterized by a rotation (tilt) of the octahedra around the *b*-axis. The room-temperature structural parameters are summarized in Table 1. The temperature evolution has been investigated in a combination of neutron (room temperature and below) and X-ray (room temperature and above) diffraction techniques. It appears that the *I*4/*mcm* or *Ibmm* phases undergo structural transitions at high temperatures and the compounds reach finally the simple perovskite phase of cubic *Pm*3*m* symmetry. On the other hand, on cooling below room temperature, the itinerant, doubly degenerate electrons of manganese 3d(e_g) character evoke different types of orbital polarization and magnetic ordering. The magnetic ground state is ferromagnetic (FM) for $x < 0.48$, A-type antiferromagnetic (AFM) for $x \sim 0.48-0.60$, and C-type AFM for $x \sim 0.60-0.75$. In the case of the A type, the tetragonal *I*4/*mcm* symmetry is reduced to the orthorhombic *Fmmm* one (in a doubled cell) upon the orbital polarization of the $d_{x^2-y^2}$ kind while for the C-type the symmetry *I*4/*mcm* is retained and only the tetragonal deformation is markedly enhanced due to polarization of the $d_{z^2-r^2}$ kind (see, for example, Figure 15 in ref 11 for details). Complete structural data at 10 K, obtained by neutron diffraction, are given in Table 2.

The dependence of lattice parameters on temperature for selected samples and corresponding space groups are displayed in Figure 1. The ordered magnetic moments in three low-temperature phases (FM, A-type, and C-type AFM) are shown in Figure 2. These results, combined with some previously published data,[12] allow us to construct a complete phase diagram of $Pr_{1-x}Sr_xMnO_3$ ($x = 0.45-0.75$), which is displayed in Figure 3. The part for $x \geq 0.6$ is rather simple and exhibits a single structural transition from the tetragonal *I*4/*mcm* to cubic *Pm*3*m* perovskite phase. The temperature of the transition decreases with increasing *x* from 775 K

(5) Pollert, E.; Jirák, Z.; Hejtmánek, J.; Strejc, A.; Kužel, R.; Hardy V. *J. Magn. Magn. Mater.* **2002**, *246*, 290.
(6) Jirák, Z.; Hejtmánek, J.; Pollert, E.; Martin, C.; Maignan, A.; Raveau, B.; Savosta, M. M.; Tomioka, Y.; Tokura, Y. *J. Appl. Phys.* **2001**, *89*, 7404.
(7) Kolesnik, S.; Dabrowski, B.; Chmaissem, O.; Bukowski, Z.; Mais, J. *J. Appl. Phys.* **2001**, *89*, 7407.
(8) Chmaissem, O.; Dabrowski, B.; Kolesnik, S.; Mais, J.; Jorgensen, J. D.; Short, S. *Phys. Rev. B* **2003**, *67*, 094431.
(9) Hejtmánek, J.; Pollert, E.; Jirák, Z.; Sedmidubský, D.; Strejc, A.; Maignan, A.; Martin, C.; Hardy, V.; Kužel, R.; Tomioka, Y. *Phys. Rev. B* **2002**, *66*, 014426.
(10) Hejtmánek, J.; Jirák, Z.; Maryško, M.; Martin, C.; Maignan, A.; Hervieu, M.; Raveau, B. *Phys. Rev. B* **1999**, *60*, 14057.
(11) Martin, C.; Maignan, A.; Hervieu, M.; Raveau, B.; Jirák, Z.; Kurbakov, A.; Trounov, V.; André, G.; Bourée, F. *J. Magn. Magn. Mater.* **1999**, *205*, 184.
(12) Martin, C.; Maignan, A.; Hervieu, M.; Raveau, B. *Phys. Rev. B* **1999**, *60*, 12191.

Table 1. Structural Parameters of $Pr_{1-x}Sr_xMnO_3$ at $T = 300$ K by Neutron and X-ray Diffraction[a]

		$x = 0.45$[b] *Ibmm*	$x = 0.48$[b] *I4/mcm*	$x = 0.50$ *I4/mcm*	$x = 0.54$ *I4/mcm*	$x = 0.60$ *I4/mcm*	$x = 0.65$[b] *I4/mcm*	$x = 0.70$ *I4/mcm*	$x = 0.75$[c] *I4/mcm*	$x = 0.85$ *Pm3m*
	a (Å)	5.4826(2)	5.4076(3)	5.4038(3)	5.3956(2)	5.3872(2)	5.3798(2)	5.3732(1)	5.3700(2)	3.8156(3)
	b (Å)	5.4380(3)	5.4076(3)	5.4038(3)	5.3956(2)	5.3872(2)	5.3798(2)	5.3732(1)	5.3700(2)	3.8156(3)
	c (Å)	7.6517(4)	7.7830(6)	7.7872(5)	7.7864(3)	7.7838(3)	7.7802(3)	7.7748(3)	7.7567(5)	3.8156(3)
	V (Å^3) [d]	57.03	56.90	56.85	56.67	56.47	56.30	56.12	55.92	55.55
	c:*a*		1.018	1.019	1.020	1.022	1.023	1.023	1.021	1
Pr,Sr	*x*	−0.0059(8)	0	0	0	0	0	0	0	0.5
	y	0	0.5	0.5	0.5	0.5	0.5	0.5	0.5	0.5
	z	0.25	0.25	0.25	0.25	0.25	0.25	0.25	0.25	0.5
Mn	*x*	0.5	0	0	0	0	0	0	0	0
	y	0	0	0	0	0	0	0	0	0
	z	0	0	0	0	0	0	0	0	0
O1	*x*	0.020(7)	0	0	0	0	0	0	0	0.5
	y	0.5	0	0	0	0	0	0	0	0
	z	0.25	0.25	0.25	0.25	0.25	0.25	0.25	0.25	0
O2	*x*	0.25	0.292(2)	0.2832(8)	0.2818(1)	0.2786(1)	0.274(1)	0.2732(1)	0.2687(6)	
	y	0.75	0.792(2)	0.7832(8)	0.7818(1)	0.7786(1)	0.774(1)	0.7732(1)	0.7687(6)	
	z	0.020(3)	0	0	0	0	0	0	0	
Mn−O1 (Å)		1.916(2) ×2	1.946(1) ×2	1.947(1) ×2	1.947(1) ×2	1.946(1) ×2	1.945(1) ×2	1.944(1) ×2	1.939(2) ×2	1.908(1) ×6
Mn−O2 (Å)		1.936(2) ×4	1.939(9) ×4	1.927(7) ×4	1.923(1) ×4	1.917(1) ×4	1.911(7) ×4	1.908(1) ×4	1.904(4) ×4	
Mn−O1−Mn (deg)		174(2) ×1	180 ×1	180 ×1	180 ×1	180 ×1	180 ×1	180 ×1	180 ×1	180 ×3
Mn−O2−Mn (deg)		171(1) ×2	161(1) ×2	164.9(5) ×2	165.5(1) ×2	167.0(1) ×2	169(1) ×2	169.4(1) ×2	171.4(3) ×2	
R_{Bragg} (%)		8.25	8.70	4.64	4.83	3.99	7.54	3.67	2.85	3.01
R_{wp} (%)		13.3	13.5	7.27	6.76	5.90	12.7	6.86	9.43	7.51

[a] Lattice parameters were determined by X-ray diffraction. [b,c] Atom positions were determined by an X-ray diffractometer and a G41 neutron diffractometer; all others were determined by a 3T2 neutron diffractometer. [d] Volume per formula unit.

Table 2. Structural Parameters of $Pr_{1-x}Sr_xMnO_3$ at $T = 10$ K by Neutron Diffraction

		$x = 0.50$ *Fmmm*	$x = 0.54$ *Fmmm*	$x = 0.60$ *Fmmm* (93%)	$x = 0.60$ *I4/mcm* (7%)	$x = 0.70$ *I4/mcm*	$x = 0.75$[a] *I4/mcm*	$x = 0.85$[11] *I4/mcm*
	a (Å)	7.5158(3)	7.5140(3)	7.5161(3)	5.3370(8)	5.3297(3)	5.3371(5)	5.3431(3)
	b (Å)	7.8359(5)	7.8143(3)	7.7928(3)	5.3370(8)	5.3297(3)	5.3371(5)	5.3431(3)
	c (Å)	7.6872(5)	7.6784(4)	7.6587(3)	7.8687(15)	7.8573(4)	7.8085(15)	7.7363(5)
	V (Å^3) [b]	56.59	56.36	56.07	56.03	55.80	55.61	55.22
Pr,Sr	*x*	0	0	0	0.5	0.5	0.5	0.5
	y	0.2506(18)	0.2507(2)	0.2507(2)	0	0	0	0
	z	0	0	0	0.25	0.25	0.25	0.25
Mn	*x*	0.25	0.25	0.25	0	0	0	0
	y	0	0	0	0	0	0	0
	z	0.25	0.25	0.25	0	0	0	0
O1	*x*	0.2135(17)	0.2161(2)	0.2188(1)	0	0	0	0
	y	0	0	0	0	0	0	0
	z	0	0	0	0.25	0.25	0.25	0.25
O2	*x*	0	0	0	0.2844(9)	0.2798(1)	0.2748(5)	0.2671(2)
	y	0	0	0	0.7844(9)	0.7798(1)	0.7748(5)	0.7671(2)
	z	0.2879(15)	0.2853(1)	0.2822(1)	0	0	0	0
O3	*x*	0.25	0.25	0.25				
	y	0.25	0.25	0.25				
	z	0.25	0.25	0.25				
Mn−O1 (Å)		1.941(2) ×2	1.936(1) ×2	1.929(1) ×2	1.967(1) ×2	1.964(1) ×2	1.952(1) ×2	1.934(1) ×2
Mn−O2 (Å)		1.901(2) ×2	1.898(1) ×2	1.895(1) ×2	1.905(5) ×4	1.898(1) ×4	1.896(3) ×4	1.894(1) ×4
Mn−O3 (Å)		1.959(1) ×2	1.954(1) ×2	1.948(1) ×2				
Mn−O1−Mn (deg)		163.8(8) ×1	164.9(1) ×1	166.0(1) ×1	180 ×1	180 ×1	180 ×1	180 ×1
Mn−O2−Mn (deg)		162.4(7) ×1	163.6(1) ×1	165.1(1) ×1	164.3(4) ×2	166.4(1) ×2	168.7(2) ×2	172.2(1) ×2
Mn−O3−Mn (deg)		180 ×1	180 ×1	180 ×1				
R_{Bragg} (%)		4.64	2.77	2.74	5.22	3.05	2.96	3.54
R_{wp} (%)		7.27	6.05	5.30	7.48	9.46	10.2	

[a] G41 neutron diffractometer; otherwise, 3T2 neutron diffractometer. [b] Volume per formula unit.

for $x = 0.6$ and remains slightly above the room temperature for $x = 0.75$. However, for higher Sr content the temperature of the tetragonal−cubic transition decreases below room temperature.[11,13] The part of the phase diagram for $x < 0.6$ is more complicated. The room-temperature *I4/mcm* phase for $0.48 \leq x < 0.6$ transforms on heating first to *Ibmm* through a two-phase region and then it is changed to $R\bar{3}c$ and finally to *Pm3m*. The existence of the two-phase region (*Ibmm* + *I4/mcm*) was tested, in particular, by measuring more scans for $x = 0.54$ while keeping the temperature at $T = 620$ K. The transition temperatures, observed for the $x = 0.48$ sample, are $T_{tetra-ortho} = 305-325$ K, $T_{ortho-rho} = 510$ K, and $T_{rho-cub} = 1140$ K, respectively. The samples with slightly lower *x* possess the orthorhombic

(13) Martin, C.; Maignan, A.; Hervieu, M.; Raveau, B.; Jirák, Z.; Savosta, M. M.; Kurbakov, A.; Trounov, V.; André, G.; Bourée, F. *Phys. Rev. B* **2000**, *62*, 6442.

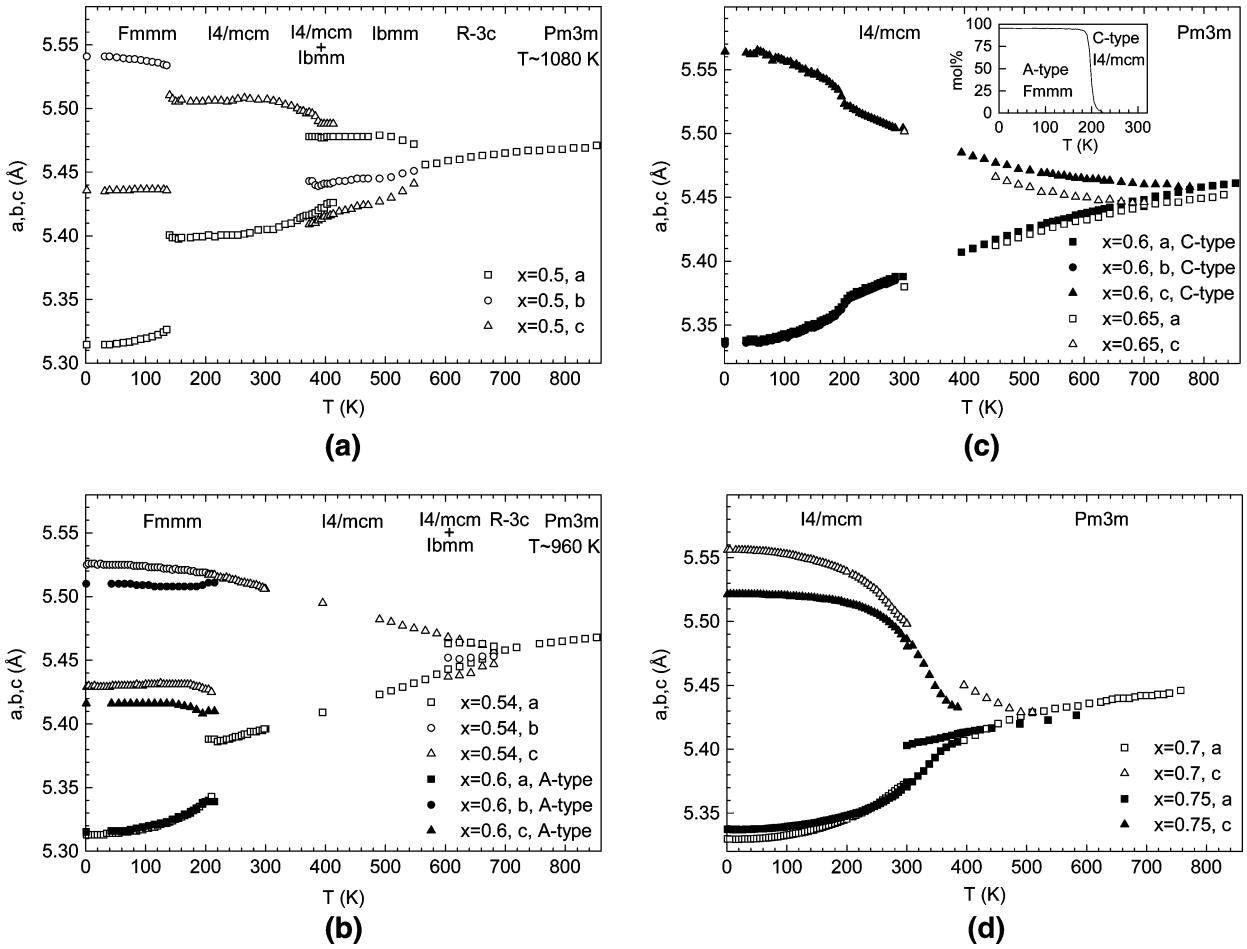

Figure 1. Temperature dependence of lattice parameters in $Pr_{1-x}Sr_xMnO_3$. The displayed parameters *a*, *b*, and *c* are renormalized with respect to individual space groups with different formula units (*Z*) to fit into the selected range. The actual lattice parameters are for *Fmmm* ($Z = 8$): $a \times \sqrt{2}$, $b \times \sqrt{2}$, $c \times \sqrt{2}$; *I*4/*mcm* ($Z = 4$): a (=b), $c \times \sqrt{2}$; *Ibmm* ($Z = 4$): a, b, $c \times \sqrt{2}$; $R\bar{3}c$ ($Z = 2$): a (=b = c), $\alpha > 60°$ is given below in Figure 4; *Pm*3*m* ($Z = 1$): $a/\sqrt{2}$ (= $b/\sqrt{2} = c/\sqrt{2}$).

structure already in the ground state. For $x = 0.45$, the low-temperature symmetry *Ibmm* changes to rhombohedral $R\bar{3}c$ at 500 K and to the cubic *Pm*3*m* at around 1260 K.

The $R\bar{3}c$ region for $x < 0.6$ at elevated temperatures deserves more attention. The dependence of the rhombohedral angle on temperature is displayed in Figure 4. To estimate the shape of the $R\bar{3}c$ region at smaller *x*, we have also included a measurement for $x = 0.3$. For a particular temperature, the rhombohedral distortion gradually increases with decreasing *x*. A striking property is a very regular linear decrease of the rhombohedral angle with temperature, exhibiting similar slope for all the compounds. This allows derivation of the transition from $R\bar{3}c$ to *Pm*3*m* more reliably by means of the extrapolation of the rhombohedral angle to $\alpha = 60°$ in addition to analyzing the diffraction profiles. The $R\bar{3}c$ area at elevated temperatures is dominant for samples close to the orthorhombic−tetragonal boundary at $x \sim 0.48$. It is gradually reduced for lower *x*, according to our measurement on $x = 0.3$, and no $R\bar{3}c$ phase is evidenced for $x = 0$.[14] This points to an increasing role of Jahn−Teller effect to the stabilization of the *Pbnm* phase, associated with the increasing concentration of Mn^{3+} ions. It is worth mentioning that the high-temperature phase of the $R\bar{3}c$ symmetry was also observed for quenched samples $Pr_{0.5}Sr_{0.5}MnO_3$ in ref 15.

All the structural transitions encountered in the $Pr_{1-x}Sr_xMnO_3$ series are associated with a rearrangement of the MnO_6 tilts in the perovskite structure. Despite this, the unit cell volumes expand with temperature without any marked steps and the averaged linear thermal expansion coefficient above room temperature is similar for all compositions, $\alpha \sim 13(1) \times 10^{-6}$ K^{-1}.

Magnetic Ordering-Neutron Data. The samples $Pr_{1-x}Sr_xMnO_3$ with $x \leq 0.48$ are pure ferromagnets with Curie temperature $T_C \sim 290$ K. The magnetic moments are oriented along the *b*-axis of the *Pbnm* or *Ibmm* cell and for the tetragonal *I*4/*mcm* compound $x = 0.48$ along the *c*-axis. In some single crystals and other possibly nonstoichiometric samples the critical temperature may reach somewhat higher value, $T_C \sim 300$ K. The FM phase is realized also for $x = 0.49-0.54$ at intermediate temperatures while a second transition to the A-type AFM state takes place at lower temperatures ($T_C = 265$ K, $T_N = 140$ K for $x = 0.5$). This AFM ground state is characterized by the orthorhombic *Fmmm* symmetry and consists of an AFM stacking of FM layers perpendicular to the *a*-axis. The magnetic moments alternate

(14) Jirák, Z.; Pollert, E.; Andersen, A. F.; Grenier, J.-C.; Hagenmuller, P. *Eur. J. Solid State Inorg. Chem.* **1990**, *27*, 421.

(15) Boujelben, W.; Ellouze, M.; Cheikh-Rouhou, A.; Pierre, J.; Joubert, J. C. *J. Solid State Chem.* **2002**, *165*, 375.

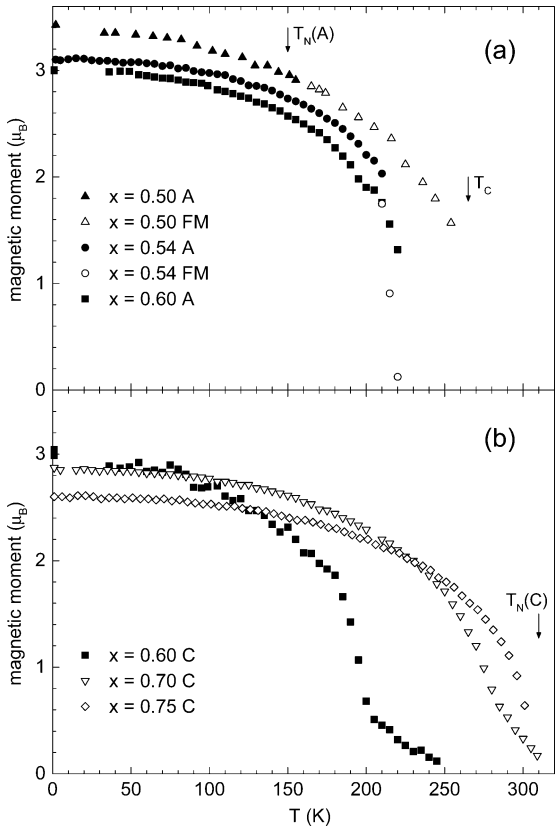

Figure 2. Temperature dependence of ordered magnetic moments in FM, A-type, and C-type AFM ground states of $Pr_{1-x}Sr_xMnO_3$.

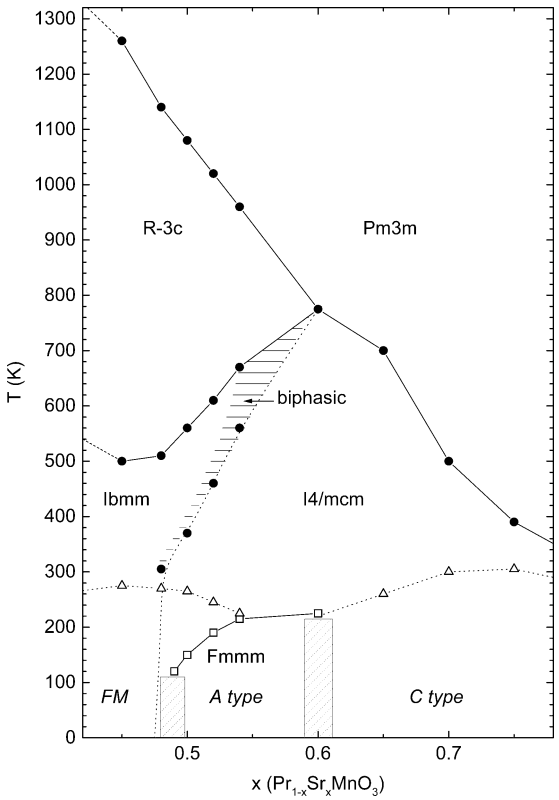

Figure 3. Phase diagram of $Pr_{1-x}Sr_xMnO_3$ ($0.45 \leq x \leq 0.75$) in air.

plus and minus in the orthorhombic *b*-direction that coincides with the *c*-axis of the original *I*4/*mcm* phase. A previous report shows that for $x = 0.55-0.58$ the onset

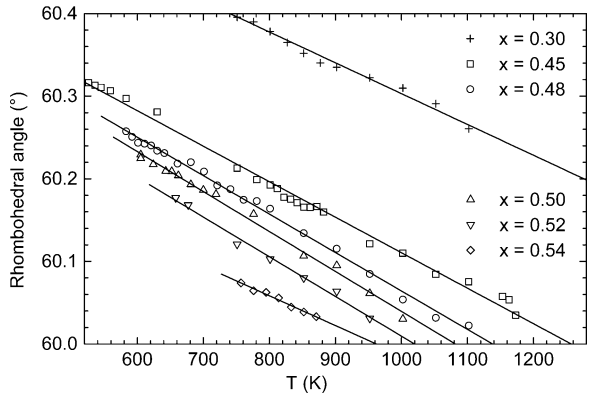

Figure 4. Temperature dependence of the rhombohedral angle in $R\bar{3}c$ phases.

of the A-type antiferromagnetism and *Fmmm* transition occurs directly from the paramagnetic state at $T_N = 215$ K.[12]

The sample with $x = 0.6$ is borderline between two antiferromagnetic ground states, the A-type (*Fmmm* phase) and C-type (*I*4/*mcm* phase). The C-type ordering develops below a critical temperature $T_{N1} \sim 250$ K while first signs of the *I*4/*mcm*−*Fmmm* phase transition and A-type ordering are evidenced at $T_{N2} = 220$ K. The *Fmmm* ratio increases very steeply around 200 K and is quickly saturated at about 93% (see the inset of Figure 1c). At the same temperature, the C-type ordered magnetic moments in the remaining *I*4/*mcm* regions increase markedly as shown in Figure 2b. This is a signature of an electronic separation that stabilizes the biphasic state. Similar effects were observed earlier for the C- and G-type phase coexistence in $Pr_{0.1}Sr_{0.9}MnO_3$.[13]

The samples $Pr_{1-x}Sr_xMnO_3$ in the region $0.65 \leq x \leq 0.85$ are pure C-type antiferromagnets of the *I*4/*mcm* crystal structure. Néel temperature reaches a maximum of $T_N \sim 305$ K for $x = 0.75$. It is worth mentioning that the $x = 0.85$ sample shows similarly strong AFM interactions, but the C-type ordering vanishes concurrently with the *I*4/*mcm*−*Pm*3*m* structural transition at a rather low temperature of 260 K.[16]

Magnetic Susceptibility. The above-mentioned neutron diffraction data on the magnetic ordering are complemented by measurements of magnetic susceptibility. The low-temperature data are displayed in Figure 5. For $x = 0.5$, a bulk ferromagnetism is evidenced at intermediate temperatures $T = 140-265$ K ($\chi \sim 10$ emu·mol^{-1}). The FM state is present also for $x = 0.54$, but in a much narrower temperature range ($T = 210-220$ K). The transition to the A-type AFM ground state and orbitally ordered *Fmmm* phase for samples $x = 0.5-0.6$ is manifested with a sharp drop of the susceptibility. On the other hand, the C-type ordering for $x = 0.7$ and 0.75 is less obvious in the susceptibility data. Of interest is a small hump noticeable thanks to the logarithmic scales of Figure 5. It is situated for all samples at temperatures of 300−310 K, very close to the maximum value of both ferromagnetic and antiferromagnetic long-range order in the $Pr_{1-x}Sr_xMnO_3$ series. In our opinion, this is an important signature of a general tendency of

(16) Hervieu, M.; Martin, C.; Maignan, A.; Van Tendeloo, G.; Jirák, Z.; Hejtmánek, J.; Barnabe, A.; Thopart, D.; Raveau B. *Chem. Mater.* **2000**, *12*, 1456.

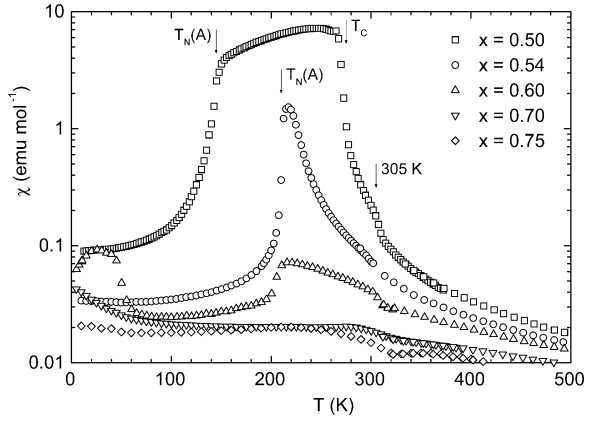

Figure 5. Logarithmic plot of magnetic susceptibility in $Pr_{1-x}Sr_xMnO_3$. The arrow shows an anomaly at 300−310 K discussed in the text.

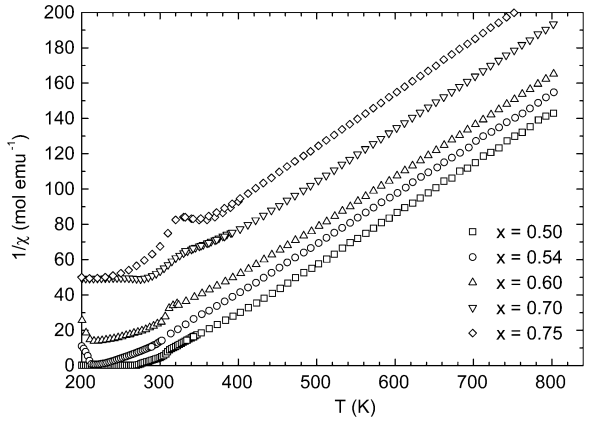

Figure 6. High-temperature reciprocal susceptibility in $Pr_{1-x}Sr_xMnO_3$.

Mn^{3+}/Mn^{4+} manganites to a charge carrier segregation at the sub-microscopic scale. This tendency can be further enhanced by introducing foreign cations on Mn sites or by another disorder.[17,18] Another marked finding is the hump of the $x = 0.6$ susceptibility at low temperatures, resembling the spin-glass transition. The susceptibility reaches a maximum of about $\chi = 0.1$ emu/mol at 30 K. A similar but much stronger peak ($\chi \sim 1$ emu/mol) was recently revealed in the $La_{0.46}Sr_{0.54}MnO_3$ system upon Cr doping at Mn sites and related to the magnetic frustration induced by the dopant.[19] In our sample $x = 0.6$, such re-entrant spin-glass behavior may originate in minor magnetically frustrated regions located possibly between the coexisting highly ordered A-type and C-type AFM domains ($m_A \sim m_C \sim 3\ \mu_B$; see Figure 2a,b).

The paramagnetic properties are best manifested in the plot of reciprocal susceptibilities in Figure 6. The curves are strictly linear in the high-temperature range and the perovskite phase transitions do not cause any anomalies. The extrapolated Curie−Weiss temperatures θ_p decrease in a very regular way as the sample composition varies from $x = 0.5$ to $x = 0.75$. Anyway, they remain positive, showing that prevailing interactions are ferromagnetic, despite the AFM ground states in $Pr_{1-x}Sr_xMnO_3$.

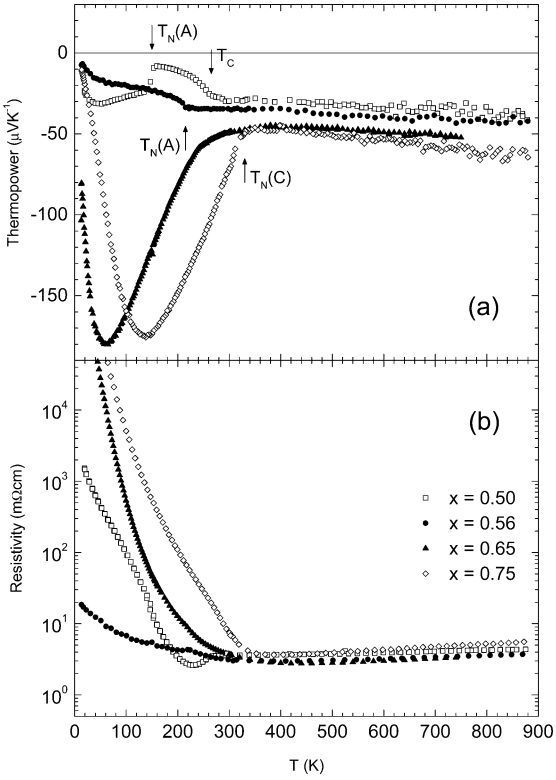

Figure 7. Thermopower coefficient (a) and resistivity (b) measured on ceramic samples $Pr_{1-x}Sr_xMnO_3$.

Transport Properties. The electric transport data in $Pr_{1-x}Sr_xMnO_3$ ($0.5 \le x \le 0.75$) are summarized in Figure 7. In the present case of ceramic samples, due to the possible impact of grain boundaries on the electrical resistivity, more significance should be given to the thermoelectric power data shown in the upper panel. In particular, the small negative values for $x = 0.5$ in the range 140−265 K evidence the metallic nature of the FM state while the slowly decreasing thermopower below the $T_N = 150$ K is a clear signature of a weak localization in the A-type ground state of that sample. On the other hand, the quasi-linear behavior below 215 K for $x = 0.56$ strongly suggests that the A-type phase in that composition range acquires a true metallicity. Other two samples with $x = 0.65$ and 0.75 show, in coherence with a quasi 1-D orbital and magnetic C-type ground state, the significant charge carrier localization characterized by high absolute values of the thermoelectric power.

The resistivity and thermopower data at elevated temperatures show a quasi-linear (metallic-like) dependence that is very similar for all the samples and does not reflect the structural transitions toward the cubic perovskite *Pm*3*m* phase.

Conclusion

Structural, magnetic, and electric transport investigations have been performed on perovskite manganites $Pr_{1-x}Sr_xMnO_3$ ($0.45 \le x \le 0.75$). The observed data include both the low-temperature range with occurrence of three magnetically ordered phases (FM, A-type, and C-type AFM) and the high-temperature range up to

(17) Jirák, Z.; Hejtmánek, J.; Knížek, K.; Maryško, M.; Martin, C.; Maignan, A.; Hervieu, M. *J. Appl. Phys.* **2003**, *93*, 8083.
(18) Knížek, K.; Jirák, Z.; Hejtmánek, J.; Maryško, M.; Martin, C.; Maignan, A.; Hervieu, M. *J. Magn. Magn. Mater.*, in press.
(19) Dho, J.; Kim, W. S.; Hur, N. H. *Phys. Rev. Lett.* **2002**, *89*, 027202.

1200 K where the room-temperature perovskite structures (orthorhombic *Ibmm* for $x < 0.48$ and tetragonal *I*4/*mcm* for $x > 0.48$) undergo phase transitions toward the simple cubic perovskite structure. The refined phase diagram shows that for $x \geq 0.6$ the *I*4/*mcm* structure transforms directly to the cubic *Pm*3*m*. The temperature behavior for lower x is more complicated. First, the tetragonal *I*4/*mcm* compounds with $x < 0.6$ transform on heating to the *Ibmm* structure through a two-phase region, and then the orthorhombic structure transforms to the rhombohedral $R\bar{3}c$ before the final transition to the simple perovskite structure *Pm*3*m*. The $R\bar{3}c$ area at elevated temperatures is dominant for samples close to the orthorhombic−tetragonal boundary $x \sim 0.48$ and is gradually reduced for lower x.

Despite the richness of perovskite phases and magnetic ground states, the magnetic interactions at high temperatures point to a dominance of a single ferromagnetic coupling which should be attributed to the Mn^{3+}/Mn^{4+} pairs and, consequently, gives maximum Curie−Weiss temperature θ_p for $x \sim 0.5$. The transport properties, manifested more readily in the thermopower data because of ceramic character of the samples, are sensitive to the magnetic transitions and associated changes of orbital polarization of charge carriers at low temperatures. At high temperatures, on the other hand, the structural transitions have little effect on thermopower and resistivity and the dependence on x is practically smeared out.

Acknowledgment. The authors acknowledge A. Maignan for discussions and N. Nguyen for Faraday balance measurement. The work was supported in part by the European Community's Human Potential Program under Contract HPRN-CT-2002-00293, SCOOTMO. The work in the Institute of Physics was performed within the research plan of Academy of Sciences AVOZ1-010-914.

CM034997R